Tectonophysics 870 (2024) 230160

Contents lists available at ScienceDirect

Tectonophysics

journal homepage: www.elsevier.com/locate/tecto

A petrophysical study of the composition of Taiwan's middle and lower crust

D. Brown [a,c,*], G. Camanni [b], H. Kuo-Chen [c], J. Alvarez-Marron [a]

[a] Geosciences Barcelona, CSIC, 08028 Barcelona, Spain
[b] DiSTAR, Università degli Studi di Napoli "Federico II", Naples, Italy
[c] Department of Geosciences, National Taiwan University, 10617 Taipei, Taiwan

ARTICLE INFO

Keywords:
Taiwan
Petrophysics
Seismic wavespeeds
Composition of the middle and lower crust
Mafic

ABSTRACT

A first-order approximation of the lithological make-up of an orogen's middle and lower crust can provide insights into its structure, as well as the tectono-metamorphic and geodynamic processes taking place there. In this study, we investigate the possible lithological and chemical composition of Taiwan's middle and lower crust by matching in situ physical properties measured by the TAIGER tomography data with isotropic wavespeeds, density, and major element composition for a variety of upper amphibolite and granulite facies rocks modelled at ambient pressure and temperature using the AbersHacker Macro. The modelling suggests that Taiwan's middle crust is possibly comprised of some combination of biotite-poor metapelite, garnet-poor felsic granulite, mafic granulite, amphibolite, and marble. The lower crust is likely comprised of mafic granulite, garnet-rich felsic granulite, biotite-free metapelite, and eclogite. Furthermore, the modelling shows that the modal abundance of garnet and/or sillimanite has a significant effect on physical properties, elevating seismic wavespeeds and density of felsic rocks to those of mafic rocks. The modelled wt% major oxide composition suggests that Taiwan's middle and lower crust have a more mafic chemical composition than that of global compilations of the continental crust. Nevertheless, this reflects the choices made when assigning rock types for the lithological mix used to calculate the wt% oxides, since increasing the percentage of garnet-rich metapelite and felsic granulite would result in a more felsic bulk composition.

1. Introduction

Having a first-order approximation of the lithological make-up of an orogen's middle and lower crust can provide insights into its structure, as well as the tectono-metamorphic and geodynamic processes that are possibly taking place deep within the crust (e.g., Morozov et al., 2003; Marini and Manzella, 2005; Brownlee et al., 2011; Brown et al., 2015; Peng and Redfern, 2013; Zappone and Benson, 2013; Taylor et al., 2015). Compositional modelling of rock physical properties (body wave velocities and density) is a widely used tool for investigating the in situ nature of the deep crust (e.g., Holbrook et al., 1992; Christensen and Mooney, 1995; Rudnick and Fountain, 1995; Kern et al., 1996; Hyndman and Peacock, 2003; Rudnick and Gao, 2003; Hacker et al., 2015). Such modelling is typically based on matching in situ P- and S-wave velocities (Vp and Vs, respectively), and density obtained from seismic refraction and tomography experiments with laboratory measurements of these obtained from samples of known mineral and chemical composition (e.g., Holbrook et al., 1992; Miller and Christensen, 1994; Christensen and Mooney, 1995; Rudnick and Fountain, 1995; Kern et al., 1996; Morozov et al., 2003; Rudnick and Gao, 2003; Brown et al., 2003, 2015; Brownlee et al., 2011; Llana-Funez and Brown, 2012). There are, however, important uncertainties involved in the calculation of crustal composition in this way. Primary among these is the non-uniqueness of rock physical properties; several lithologies can have similar P- and S-wave velocities, and density (e.g., Kern, 1982; Christensen and Mooney, 1995; Christensen, 1996; Hacker et al., 2015). A corollary to this is that the modelled chemical composition of the crust can vary significantly depending on the lithology that is chosen to match the physical properties data (e.g., Hacker et al., 2015). Further uncertainty, especially in "hot" orogens, is introduced by the fact that laboratory measurements of seismic velocities are often not carried out under pressure and temperature conditions that are sufficiently high as to effect the α-β transition in quartz (e.g., Kern, 1982; Peng and Redfern, 2013; Zappone and Benson, 2013).

* Corresponding author at: Geosciences Barcelona, CSIC, 08028 Barcelona, Spain.
E-mail address: dbrown@geo3bcn.csic.es (D. Brown).

https://doi.org/10.1016/j.tecto.2023.230160
Received 6 May 2023; Received in revised form 21 November 2023; Accepted 2 December 2023
Available online 7 December 2023

The aim of this paper is to investigate the possible lithological and chemical composition of the middle and lower crust of the active Taiwan orogen (Fig. 1). We also look at the possible mineral composition of each rock type and how this affects physical properties and chemical composition. To do this, we extract in situ P-wave and S-wave velocities, and calculate densities from the TAIGER tomography models (Kuo-Chen et al., 2012a). We then compare these with the physical properties, and mineralogical and chemical composition of a number of common rock types that we calculate using the AbersHackerMacro (AHM) (Hacker and Abers, 2003; Abers and Hacker, 2016). An advantage of using the AHM, as opposed to laboratory measurements, is that it calculates the α-β transition in quartz, which will cause important changes in the physical properties of quartz-bearing rocks (e.g., Kern, 1982; Peng and Redfern, 2013; Zappone and Benson, 2013) (Fig. 2). AHM also allows us to model rock physical properties at the pressure and temperature conditions of interest to Taiwan.

2. Geological background

Taiwan is an active mountain belt that has been forming since the Late Miocene as the result of the collision of the Luzon arc with the deeply subducting Eurasian margin (e.g., Sibuet and Hsu, 1997, 2004; Teng and Lin, 2004; Huang et al., 2014a). The part of the continental margin of the Eurasian margin that is involved in the collision is thought to have evolved from a sub-continental subduction system in the Late Cretaceous (Li et al., 2007; Lan et al., 2008) to a rifting margin by the Early Eocene followed, during the late Early Oligocene, by sea-floor spreading and, from the Late Miocene to the present, the subduction of Eurasian Plate beneath the Philippine Sea Plate (Lin et al., 2003; Huang et al., 2012). The Mesozoic pre-rift geology and lithostratigraphy of the margin area that is entering into the Taiwan mountain belt is not well known. Nevertheless, some authors suggest that it is largely comprised of variably metamorphosed felsic to mafic intrusive igneous rocks and to have been under-plated by mafic rocks during the Miocene (e.g., Chen et al., 2016; Liu et al., 2023).

The Taiwan orogen is divided into five roughly N-S oriented geological provinces that are separated by major faults (Fig. 1). From west to east these zones are: the Coastal Plain, the Western Foothills (in what follows, this includes the Coastal Plain), the Hsuehshan Range, the Central Range, and the Coastal Range (Fig. 1). In the north, the Western Foothills is juxtaposed against the Hsuehshan Range across the Shuilikeng Fault (SkF). In the east, the Hsuehshan Range is juxtaposed against

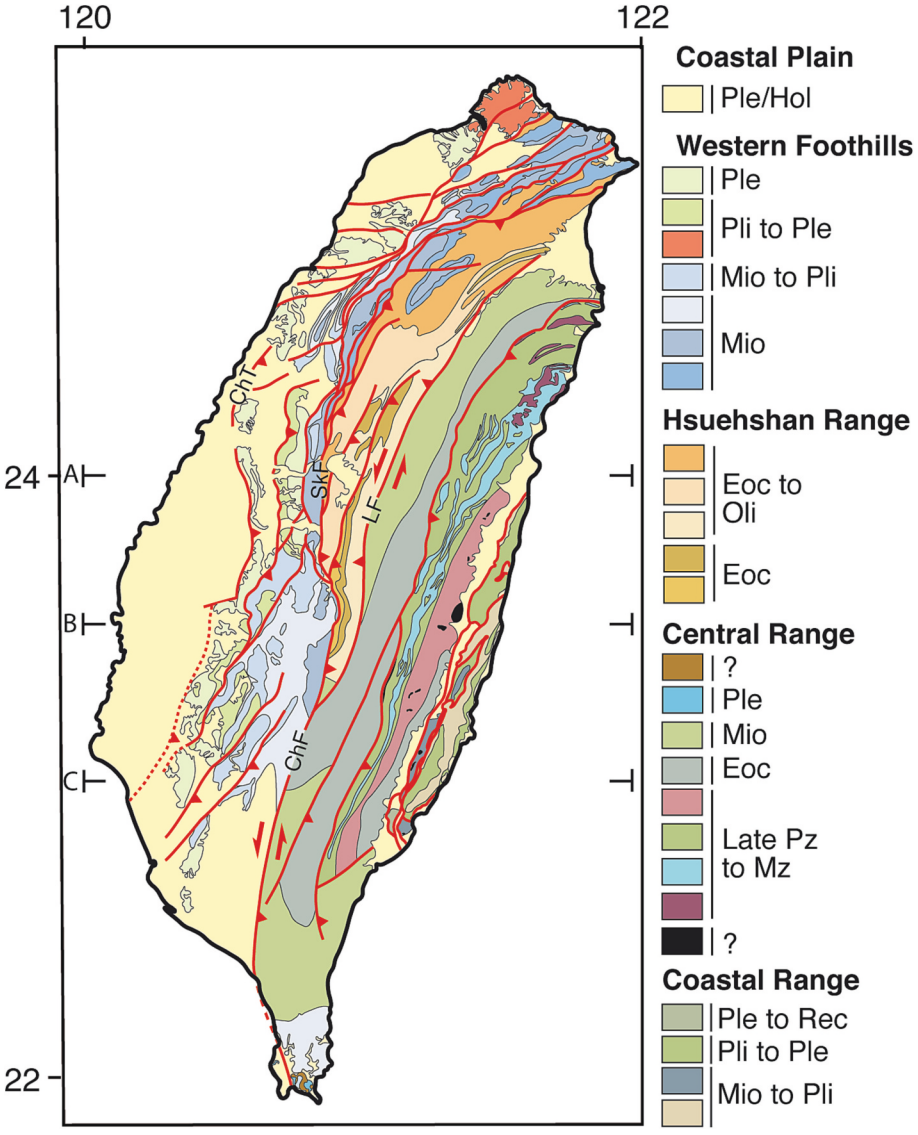

Fig. 1. Geological map of Taiwan (after Chen et al., 2000). The locations of the velocity sections (A, B, and C) given in Fig. 3 are shown. ChT = Changhua thrust, SkF = Shulikeng fault, LF = Lishan fault, ChF = Chaochou fault.

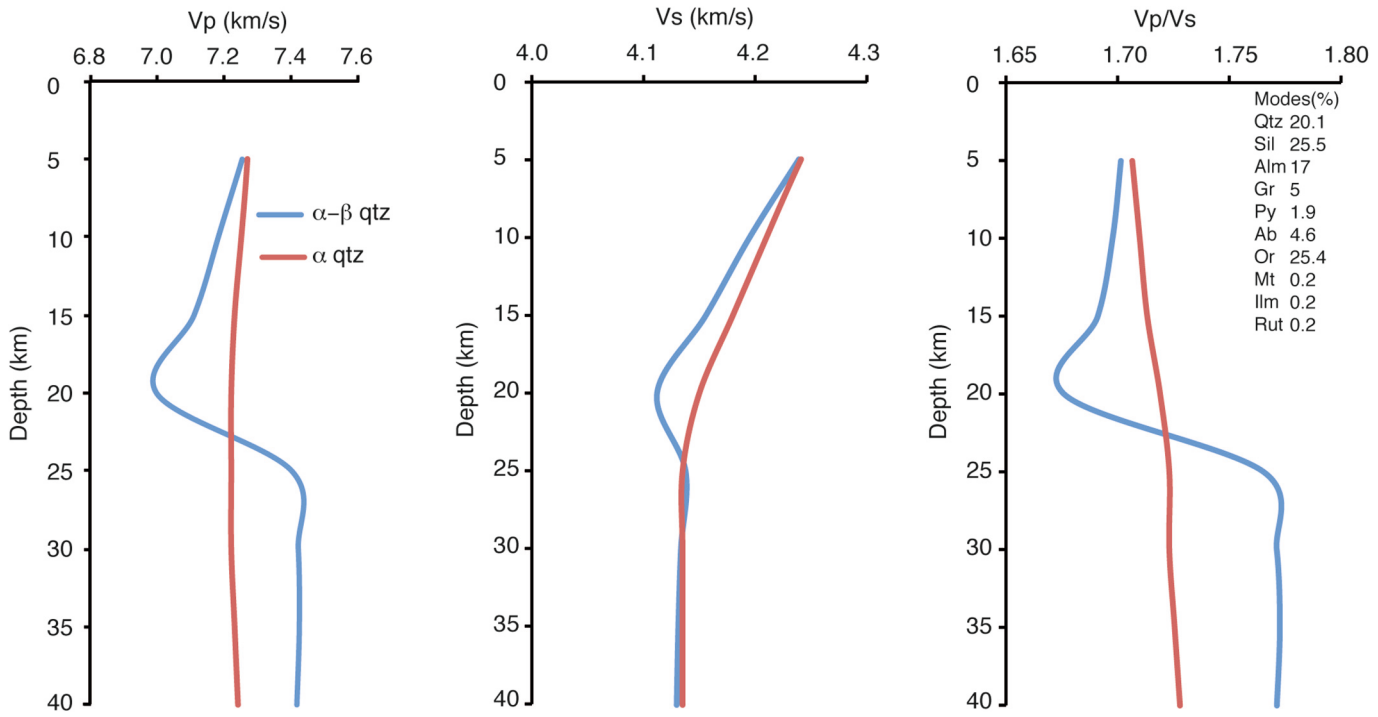

Fig. 2. Vp, Vs, and Vp/Vs versus depth functions calculated for a metapelite sample using the AHM. Values are calculated at 5 km depth intervals using the geothermal gradient in Fig. 5. The modal abundance of the constituent mineral phases is shown in the upper right. In one set of calculations, the α–β quartz transition is allowed to take place (blue line), and in the other (red line) only α quartz is present. The α–β quartz transition takes place at 20 km depth. The profiles of the depth functions are quite different, indicating the importance of taking the α–β quartz transition into consideration when carrying out petrophysical modelling of the composition of the crust. (For interpretation of the references to colour in this figure legend, the reader is referred to the web version of this article.)

the Central Range across the Lishan Fault (LF). Southward, the Shuilikeng and Lishan faults link up with one another and the Central Range is juxtaposed against the Western Foothills along the Chaochou Fault (ChF).

The outcropping geology of the Central Range is comprised predominantly of Mesozoic-age, greenschist to amphibolite facies marble, quartz-mica schist, ortho- and paragneiss, and amphibolite (Stanley et al., 1981; Ernst, 1983; Ernst and Jahn, 1987; Ho, 1988; Lan et al., 2008) (Fig. 1). Along its western flank, these are structurally overlain by lower greenschist facies, Eocene- and Miocene-age slate, phyllite, and sandstone. Along its eastern flank, the Central Range is juxtaposed against high-pressure rocks and quartz-mica schist of the Yuli Belt along the Shoufeng fault (e.g., Ernst and Jahn, 1987; Tsai et al., 2013; Ho et al., 2022). The Mesozoic rocks found in the Central Range do not crop out in the Western Foothills or Hsuehshan Range, although in western Taiwan and its offshore, several boreholes have intersected weakly metamorphosed siliciclastic and carbonate rocks that have been interpreted to range in age from Late Permian to Cretaceous (e.g., Jahn et al., 1992; Chiu, 1975; Ho, 1988; Shaw, 1996). On the basis of these boreholes, Mesozoic-aged rocks similar to those outcropping in the Central Range have been interpreted to form the basement to the Eocene and younger rocks (e.g., Brown et al., 2012, 2022). The outcropping stratigraphy of the Western Foothills and Hsuehshan Range consists of Eocene through Miocene clastic sediments of the Eurasian platform margin and latest Miocene through Holocene synorogenic sediments (e.g., Ho, 1988; Teng, 1992).

3. Velocity and density structure of Taiwan

In this paper we use the regional TAIGER P-wave (Vp) and S-wave (Vs) tomography models of Kuo-Chen et al. (2012a, 2012b), and the reader is referred there for a description of the acquisition and processing parameters, as well as details of the resolution testing. The model inversion was constructed with a 6 × 6 × 6 km grid and the ray tracing was carried out on a 3 km grid. Resolution testing indicates that it can resolve crustal and mantle features of c. 6 to >60 km (Kuo-Chen et al., 2012a). The major features imaged by the TAIGER data are also found in the Vp tomography models of Kim et al. (2005), Wu et al. (2007), and Huang et al. (2014b). Lo et al. (2021) carry out a quantitative assessment of the different tomography and indicate that the they are more similar between depths of 5 and 35 km. We expect that the features found in our velocity model are robust and can therefore be reliably interpreted. In the description of the velocity structure of Taiwan that follows, depths are given in 3 km intervals with uncertainties of ±3 km (the half-space of the grid). Throughout, uncertainties are given as 1σ of the datasets for a selected area (e.g., Western Foothills or Central Range) and specified depth. In what follows, we calculated density from Vp at each depth interval using eq. 1 of Brocher (2005). The area of interest extends from the coastline (CL in Fig. 3) in the west, through the Western Foothills, Hsuehshan Range, and Central Range to the Longitudinal Valley (LV in Fig. 3) in the east. To exclude any possible effects derived from the subduction of the Philippine Sea Plate beneath northern Taiwan (e.g., fluids (Bertrand et al., 2012)), we do not include the area to the north of 24° N.

Since the objective of this paper is to use the tomographic models to investigate the possible lithological composition of Taiwan's middle and lower crust, we define crustal domains in terms of P-wave velocity. For orogens, the middle crust is typically defined as having a P-wave velocity between 6.3 km/s and < 6.9 km/s, whereas the lower crust is 6.9 km/s and < 7.5 km/s (Christensen and Mooney, 1995; Rudnick and Fountain, 1995; Rudnick and Gao, 2003). The crust/mantle boundary (Moho) is commonly defined as a transition zone that takes place over a P-wave velocity range of 7.5 km/s to 7.8 km/s (e.g., Jarchow and Thompson, 1989; Christensen and Mooney, 1995; Giese, 2005; Carbonell et al., 2013). The mantle has a Vp >7.8 km/s.

The TAIGER P-wave velocity model indicates that there is a

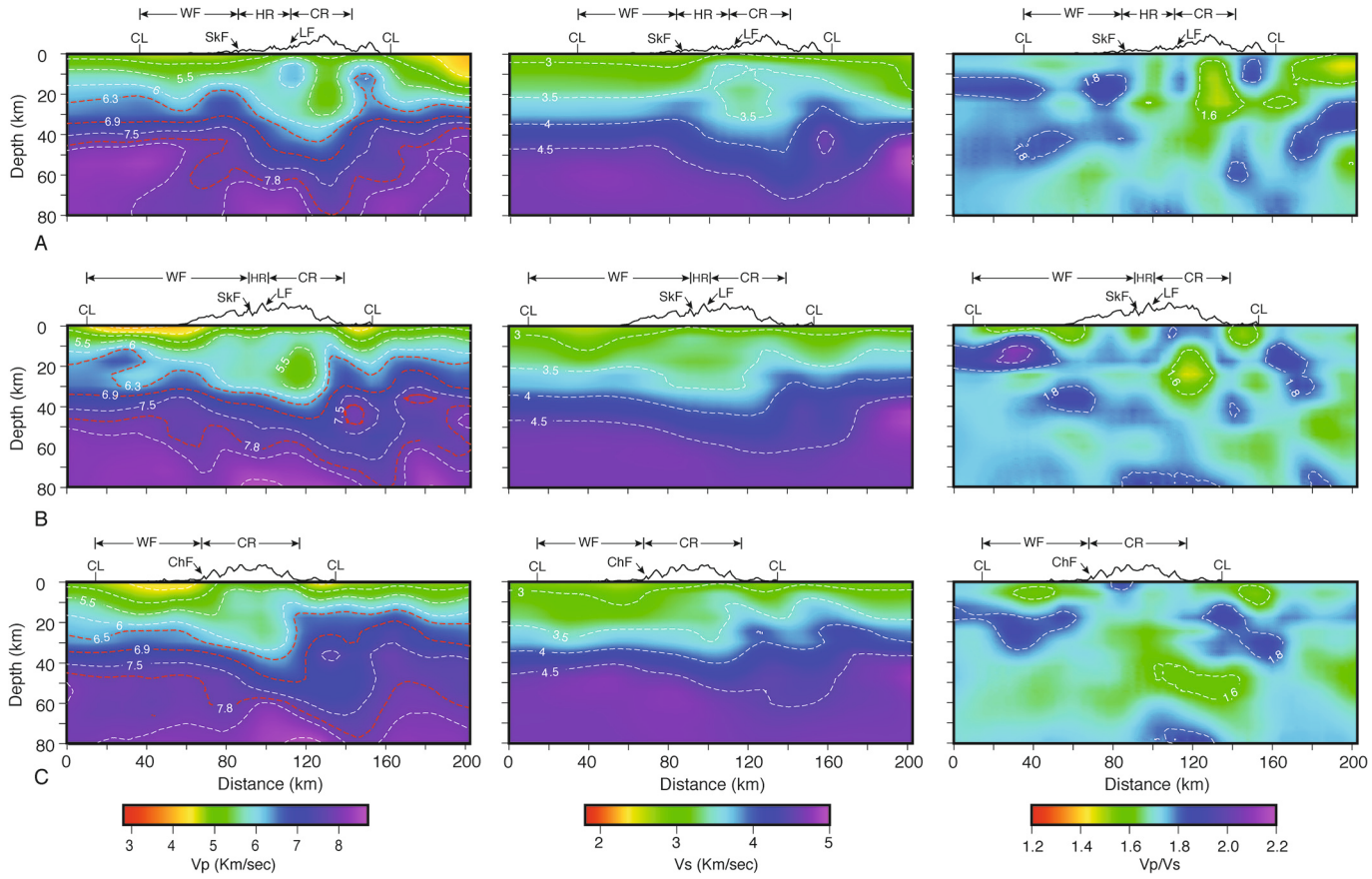

Fig. 3. Vp, Vs, and Vp/Vs sections for central and southern Taiwan (from Kuo-Chen et al., 2012a). The locations of the sections are shown in Fig. 1. WF = Western Foothills, HR = Hsuehshan Range, CR = Central Range, CL = coast line. Other labels are as in Fig. 1. In the Vp sections, the dashed red lines indicate the change from upper to middle crust (6.3 km/s), middle to lower crust (6.9 km/s), Moho transition (7.5 to 7.8 km/s). (For interpretation of the references to colour in this figure legend, the reader is referred to the web version of this article.)

significant west to east thickening of the crust (Vp <7.8 km/s) from c. 45 km beneath the Western Foothills to >60 km beneath the Central Range (WF and CR, respectively in Fig. 3). Beneath the Western Foothills, the crust has a near uniform thickness and displays a roughly subhorizontal velocity structure, with Vp and Vs increasing continuously with depth (Figs. 3 and 4). Between 9 and 18 km depth, in the middle part of the upper crust, there is a zone where Vp/Vs reaches a high of c. 1.86 (+/− 0.10) to 1.90 (+/− 0.07), and which extends across nearly the entire Western Foothills (Figs. 3 and 4). Beginning at 18 km depth, the rate of increase of Vp slows, that of Vs increases, and there is a consequent sharp decrease in Vp/Vs to 1.75 (+/− 0.04) at 24 km depth, in the upper part of the middle crust (Figs. 3 and 4). From 24 km depth, Vp and Vs increase gradually through the top of the lower crust (Vp > 6.9 km/s) at 33 km to the crust/mantle boundary at 45 km depth (Vp >7.8 km/s). Between 24 and 30 km depth, Vp/Vs remains nearly constant, increasing to 1.78 (+/− 0.05) at 36 km depth, and then it decreases continuously until 1.74 (+/− 0.04) at the crust/mantle boundary. Density increases from 2.4 to 2.8 g/cm^3 from the surface to 18 km depth, and then remains nearly constant to 33 km depth where it begins to increase again, reaching 3.2 g/cm^3 at Moho (Fig. 4D).

Eastward, beneath the Hsuehshan and Central ranges (HR and CR, respectively, in Fig. 3), the upper crust (Vp <6.3 km/s) thickens to about 36 km, and the velocity structure (especially Vp) is more complex than beneath the Western Foothills. The middle and lower crust is roughly 20 km thick, similar to that beneath the Western Foothills, but is up to 20 km deeper. In the uppermost 6 km, Vp and Vs increase to 5.8 (+/− 0.2) km/s and 3.4 (+/− 0.1) km/s, respectively (Figs. 3 and 4). Vp decreases gradually to 5.5 (+/− 0.3) km/s at 24 km depth, and then increases continuously until the crust/mantle transition (Vp >7.8 km/s) at roughly 60 km depth. Vs increases gradually throughout the middle and lower crust. The Vp/Vs ratio shows an overall patchy distribution, with values ranging from 1.60 to c.1.80 (Figs. 3 and 4). The average Vp/Vs decreases from 1.77 (+/− 0.06) at the surface to a minimum of 1.55 (+/− 0.07) at 24 km depth, increases to 1.71 (+/− 0.04) near the base of the middle crust, and then remains nearly constant until the crust/mantle transition (Figs. 3 and 4). Density increases to c. 2.7 g/cm^3 at 6 km depth and then decreases slowly to about 2.6 g/cm^3 at 24 km depth where it starts to increase, reaching about 3.1 g/cm^3 at the Moho (Fig. 4D).

4. Petrophysical modelling

4.1. Methodology

4.1.1. Geothermal gradient

Measured surface heat flow in Taiwan is relatively high (values of >100 mWm^{-2} are common), leading to calculated geothermal gradients of >50 °C/km in the Central Range and between 20 and 50 °C/km in the Western Foothills (Lee and Cheng, 1986; Wu et al., 2013). Such a high geothermal gradient results in unrealistic crustal temperatures and cannot be used in petrophysical modelling, since temperature has an important effect on the seismic velocities of rocks (e.g., Christensen and Mooney, 1995). Therefore, we determined a geothermal gradient (Fig. 5A) using a variety of published data types that measure or calculate the temperature at different depths. Constraints on the temperature for the uppermost 5 km are provided by down-hole measurements in the TCDP-A (48 °C, at 1250 m: e.g., Tanaka et al., 2007; Hung et al., 2009) and the CS-74 (177 °C, at 4661 m: Kuan (1971)) boreholes.

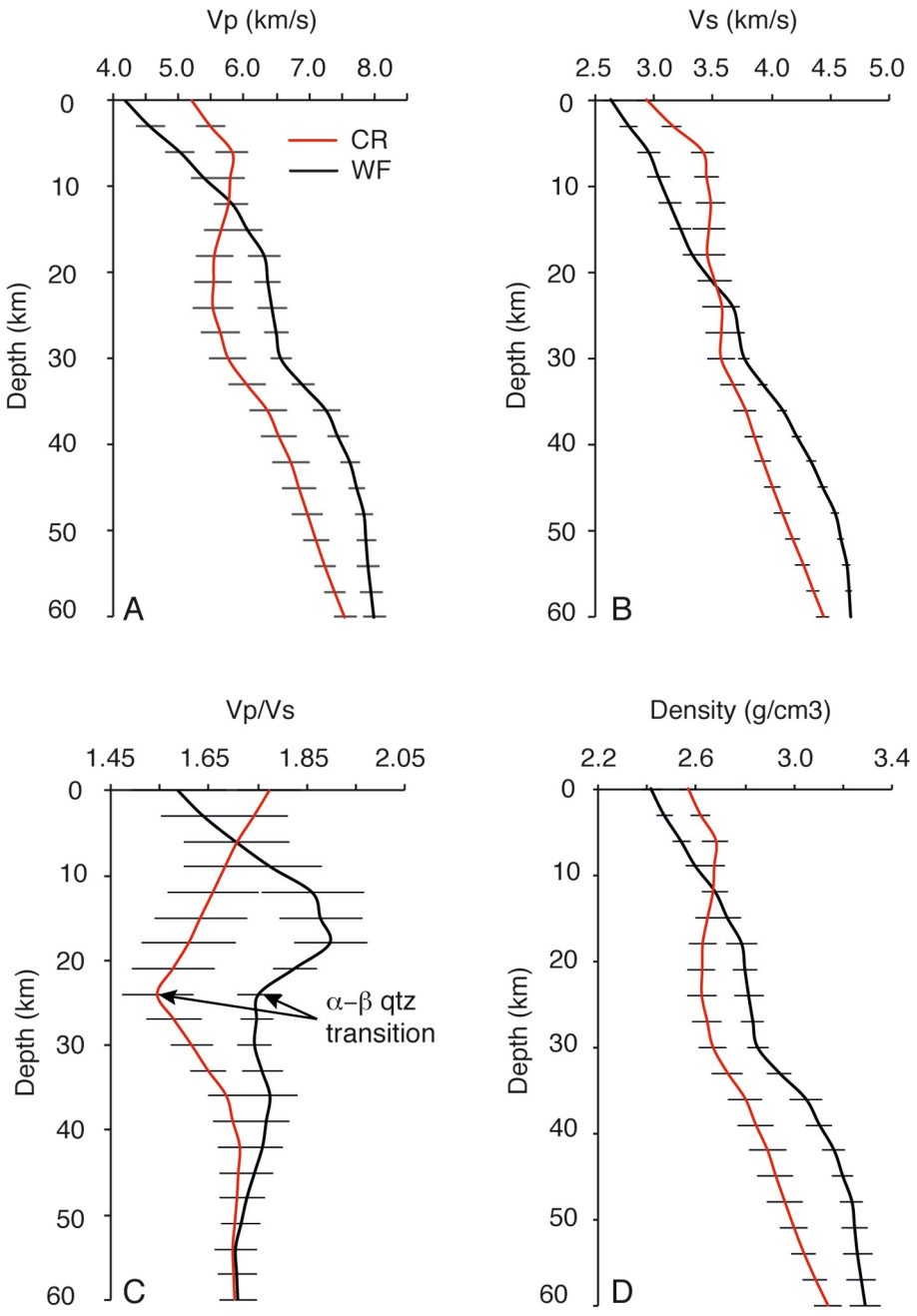

Fig. 4. Average Vp, Vs, Vp/Vs, and Density versus depth functions for the Western Foothills (WF) and the Central Range (CR) extracted from the tomography model. Error bars are 1 σ. The decrease in Vp/Vs at 24 km depth is interpreted to be the α–β quartz transition in both the Central Range (see Kuo-Chen et al., 2012b) and the Western Foothills.

For deeper crustal levels, the depth of the Curie point (580 °C at 12 +/2 km: Hsieh et al. (2014)), the α-β quartz transition in the Central Range (750 +/− 25 °C, at 24 +/3 km: Kuo-Chen et al. (2012b)), and the Pn velocity (900 ±50 °C for Pn of 7.9 km/s (+/− 0.1 km/s) at 42 ±3 km depth: Chen et al. (2003), Kuo et al. (2016)). Following Kuo-Chen et al. (2012b), we also interpret the rapid decrease in Vp/Vs at approximately 24 km depth beneath the Western Foothills to be related to the α-β quartz transition (Fig. 4C). The Pn temperature was determined using the estimates of Schutt et al. (2018), and Boyd (2020). From these data, Taiwan's middle and lower crust have a steep geothermal gradient, and are experiencing upper amphibolite to granulite facies metamorphic conditions (Fig. 5B). In the petrophysical modelling presented in Section 4, a best fit curve (R^2 = 0.982) was fitted to the geothermal gradient (Fig. 5A), and T was calculated for each 5 km interval in the model. While temperature and pressure have an important effect on seismic velocities, our models show that using values within the bounds of the uncertainties shown in Fig. 5 would result in a variation in Vp and Vs of <1%. This would not change the modelled lithological composition of the crust.

4.1.2. *Velocity, density, and composition modelling*

Modelling of physical properties and chemistry was carried out using the AbersHackerMacro (AHM in what follows) Excel spreadsheet (Hacker and Abers, 2003; Abers and Hacker, 2016), which uses the modal abundance (volume percent) of mineral end-members to build rocks and calculate their isotropic wavespeeds (Vp, Vs), density, and wt % oxide composition. In this paper, we calculate the physical properties and chemical composition for published modal abundance data from six

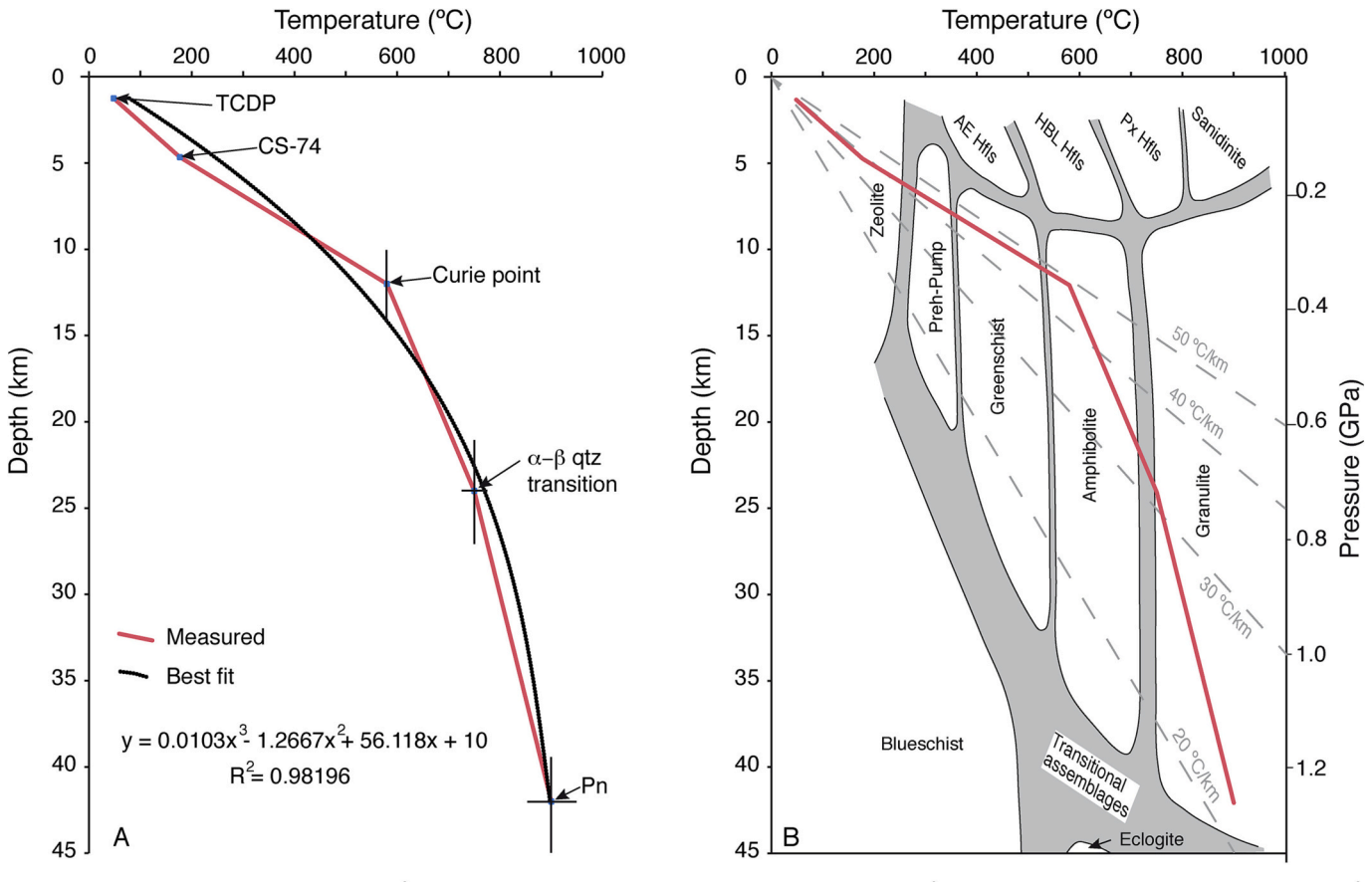

Fig. 5. A) Geothermal gradient (red) of the Western Foothills (WF) and Central Range (CR) of central and southern Taiwan determined from borehole temperature measurements (TCDP and CS-74), the Curie point, the α–β quartz transition, and the Pn velocity. Differences in the Curie point depth between the Western Foothills and the Central Range are given by the error bars (deeper is WF, shallower is CR). See Section 4.1.1 for details. The equation for the best fit curve is used to calculate the temperature at the depth of interest in the AbersHackerMacro (AHM) models (Abers and Hacker, 2016). B) The geothermal gradient indicates that, at depths of 30 km and more Taiwan's crust is currently experiencing upper amphibolite and granulite facies metamorphic conditions. (For interpretation of the references to colour in this figure legend, the reader is referred to the web version of this article.)

upper amphibolite, granulite, and eclogite facies lithologies, as well as a suite of mantle peridotite and pyroxenite rocks. To avoid geographical specificity in the samples used, we selected examples for each lithology from a number of areas. Published modal abundance data often reports the bulk mineral composition (i.e., garnet, plagioclase, or clinopyroxene) and some, but not all, of the mineral end-member compositions (i.e., almandine, pyrope, grossular). To address this, we compile a database of the major phase end-members for each lithology derived from published mineral composition data for the metamorphic conditions given above, and then use the averages of these end-member compositions in the AHM (Table 1 and Supplementary data). The garnet end-member spessartine (MnO) is not included in the AHM and was therefore not modelled. K_2O in the feldspar series was modelled as orthoclase. The Na_2O component of clinopyroxene was modelled as jadeite, and no CaO end-member was modelled for orthopyroxene. In all lithologies, amphibole was modelled as hornblende. Unless specified, the minor (often opaque) phases were modelled as equal proportions of spinel, magnetite, and ilmenite. Below, in Section 4, granulite is divided into two groups; mafic granulite (>30% pyroxene + amphibole + biotite) and felsic granulite (<30%). Metapelite is divided into two groups: those for which biotite and muscovite are absent or nearly absent (<5%: granulite facies), and those with biotite and muscovite (>5%: upper amphibolite facies). The aluminosilicate mineral in the metapelite is sillimanite. Pyroxenite (<40% olivine) and peridotite (>60% olivine) plot together as a tight cluster, and so are not shown separately. We discuss the results of these models for depths of 30, 40, and 50 km, corresponding to the middle (except in Central Range) and lower crust and the uppermost mantle. The in situ depth functions of Vp, Vs, Vp/Vs, and density for the Western Foothills and the Central Range that plotted along with the AHM models are those shown in Fig. 4.

4.1.3. *Uncertainties in the modelling*

An important uncertainty is the depth level of each velocity layer, since an underestimation of the velocity at the top of the tomography model is propagated downward into lower velocities at depth, meaning the boundaries between middle, lower crust, and mantle appear deeper than those determined from seismic refraction data (e.g., Van Avendonk et al., 2014; Kuo et al., 2016). This results in slightly elevated pressures and temperatures in the AHM models. Also, we assume that the middle and lower crust is seismically isotropic, which is not the case (Chen et al., 2003; Huang et al., 2015; Koulakov et al., 2015), and that it is dry, as is suggested by the magnetotelluric data of Bertrand et al. (2009, 2012).

A number of uncertainties accompany the AHM and the reader is referred to Hacker and Abers (2003) and Abers and Hacker (2016) for how this spreadsheet works and the uncertainties involved. The geothermal gradient calculated for Taiwan (Fig. 5A) is an uncertainty in the modelling since a number of uncertainties are introduced from determination of the Curie point, the α-β quartz transition, and the Pn depth and velocity. Nevertheless, we think that the geothermal gradient calculated in this way is more realistic than applying a linear gradient derived from surface heat flow measurements (e.g., Lee and Cheng,

Table 1
Average modal abundance of mineral end-members[a] used to calculate Vp and Vs and wt% oxides for each rock type.

		Granulite			Eclogite			Pelite			Amphibolite			Peridotite		
		Avg	std	n	Avg	std	n	Avg	std	n	Avg	std	n	Avg	std	n
Mineral	End-member															
Garnet	Almandine	50.8	10.1	166	54.1	8	101	71.3	10.0	108	55.6	3.7	21	24.1	9.4	79
	Pyrope	27.2	11.5	166	24.8	12.2	101	21.1	10.7	108	15.5	3.7	21	64.4	11.7	79
	Grossular	19.5	7.8	166	21	7.3	101	8.1	9.2	108	27	2.1	21	11.5	7.7	79
Feldspar	Albite	54.2	15.1	158	75.5	7.3	18	68.1	16.3	70	59	26	29			
	Anorthite	42	17	158	24.1	7.2	18	30.8	16.1	70	38.6	27.5	29			
	Orthoclase	3.7	10.4	158	0.4	0.4	18	1.1	1.0	70	0.8	0.6	29			
Orthopyroxene	Enstatite	61.3	9.5	84							49.4	5.2	9	90.6	2.1	87
	Ferrosilite	38.8	9.5	84							50.6	5.2	9	9.4	2.1	87
	Diopside	64.6	10	182	53.6	12.1	89				63.3	5.6	15	91.5	4.6	79
Clinopyroxene	Hedenbergite	26.2	7.5	182	8.7	7	89				36.1	5.7	15	3.4	2.4	79
	Jadeite	9.5	8.5	182	37.7	14.5	89							5.1	4.3	79
Biotite	Annite							41.6	10.9	59						
	Phlogopite							58.4	10.9	59						
Olivine	Forsterite													90.4	1.9	102
	Fayalite													9.7	1.9	102

[a] Data and references are provided in Supplementary data.

1986; Wu et al., 2013), which would mean unrealistic, high temperatures in the middle and lower crust. Nevertheless, we stress that in this study we use a single geothermal gradient and that any possible lateral variations within or from the Western Foothills and the Central Range are not taken into account. Using average end-member modal abundances introduces uncertainties because of the differences in both the velocity and composition between the modelled and the measured mineral phases. The absence of MnO in the AHM, not modelling a CaO end-member orthopyroxene, and assigning all amphibole to hornblende leads to errors in the wt% oxide composition of each modelled lithology. Finally, the modelled mineral assemblages may not be in equilibrium under the in situ pressure and temperature conditions of the Taiwan crust.

5. Results

5.1. Vp, Vs, Vp/Vs, density

At 30 km depth, the modelled velocities of mica-bearing metapelite, amphibolite, and felsic and mafic granulite correlates well with both the average in situ Vp (6.6 +/− 0.17 km/s) (uncertainties are 1σ) and Vs (3.8 +/− 0.05 km/s) measured in the middle crust of the Western Foothills (Fig. 6A). Metapelite and amphibolite, also fit well with the average Vp/Vs of 1.74 (+/− 0.04) of the Western Foothills (Fig. 6B), although felsic granulite and mafic granulite outside the range of uncertainty. The modelled densities for mica-bearing metapelite, garnet-free felsic granulite, and marble fit well with the average density (2.9 +/− 0.05 g/cm^3) (Fig. 6C). In % mineral phase vs Vp space, the modelled metapelite with up 70% mica, 30% garnet (+/−sillinanite), and up to 35% plagioclase, falls within the range of uncertainty of the in situ Vp (6.6 +/− 0.17 km/s) (Fig. 7). Felsic and mafic granulite is likely garnet-poor, can contain between 30 and 80% plagioclase, and 10 to 50% pyroxene (Fig. 7). Amphibolite can contain <10% garnet, and up to 40% of both plagioclase and pyroxene.

In the Central Range, at 30 km depth the average Vp (5.8 +/− 0.28 km/s) and Vs (3.6 +/− 0.12 km/s) are those of the upper crust (Fig. 6A). Neither Vp, Vs, Vp/Vs, nor density of the modelled lithologies fit well with those measured in the Central Range, with only low velocity, mica-bearing metapelite falling close to the range of uncertainty (Fig. 6B and C).

In the Western Foothills, at 40 km depth, the modelled velocities for the upper range of felsic and mafic granulite, biotite-poor metapelite, eclogite, and the upper range of amphibolite fit well with the in situ Vp (7.4 +/− 0.18 km/s) and Vs (4.2 +/− 0.04 km/s) (Fig. 8A). In Vp/Vs versus Vp space (Fig. 8B), metapelite and felsic and mafic granulite, eclogite, and the upper range of amphibolite are also good fits to the average Vp/Vs of 1.77 (±0.04). Only with some mica-free metapelites fit with the average density (3.1 +/− 0.06 g/cm^3) (Fig. 8C). The modelled metapelite with up to 30% garnet, between 30 and 50% garnet + sillimanite, and < 10% plagioclase fall within the range of uncertainty of the in situ Vp (7.4 +/− 0.18 km/s) (Fig. 7). Felsic and mafic granulite can contain about 30 to 40% garnet, 20 to 45% plagioclase, and 20 to 30% pyroxene. Amphibolite can contain 20 to 40% garnet, <10% plagioclase, and no pyroxene. The modelled eclogite can contain between 20 and 40% garnet, <20% plagioclase, and between roughly 10 to 40% pyroxene.

In the Central Range, at 40 km depth, the modelled velocities for mica-bearing metapelite, and amphibolite fit with the in situ average Vp (6.5 +/− 0.27 km/s) and Vs (3.9 +/− 0.08), whereas felsic and mafic granulite, and eclogite lie close to the range of uncertainty (Fig. 8A). In the Vp/Vs vs Vp space (Fig. 8B), only metapelite falls within the range of uncertainty for the measured velocities in the Central Range (1.70 ±0.04). The modelled mica-bearing metapelite, garnet-free felsic granulite, and marble fit well with the average density (2.8 +/− 0.08 g/cm^3) of the Central Range (Fig. 8C). In terms of the modelled mineralogical compositions, metapelite with up to 40% garnet (+/− sillimanite), and

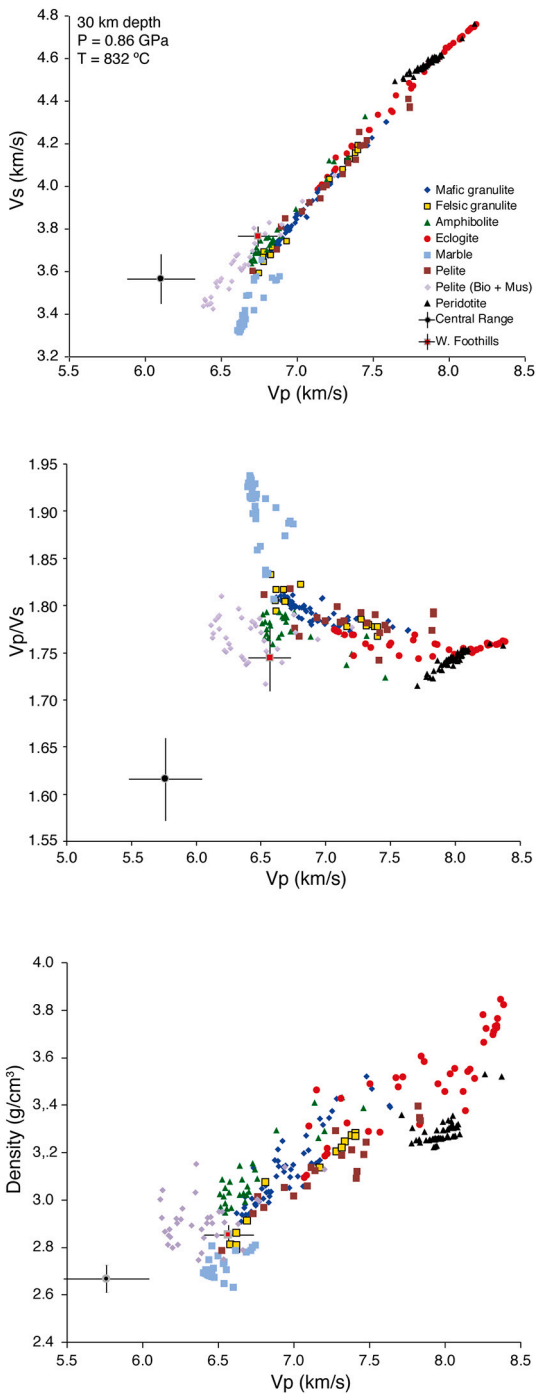

Fig. 6. Vs vs Vp, Vp/Vs vs Vp, and Density vs Vp plots for the model lithologies at 30 kn depth ($P = 0.86$ GPa) and $T = 832$ °C. The average in situ values for the Western Foothills and the Central Range are shown. Error bars are 1 σ.

up to 35% plagioclase falls within the range of uncertainty of the in situ Vp (6.5 +/− 0.27 km/s), whereas the felsic and mafic granulite are garnet-free, can contain between 30 and 80% plagioclase and 10 to 50% pyroxene (Fig. 7). Amphibolite can contain <10% garnet, and up to 40% of both plagioclase and pyroxene. Eclogite can contain between 10 and 30% garnet, 20 to 25% plagioclase, and up to roughly 30% pyroxene.

At 50 km depth in the Western Foothills, in the uppermost mantle, the modelled velocities for eclogite and peridotite (including pyroxenite) fit well with the measured averages of Vp (7.9 ±0.17 km/s) and Vs (4.6 ±0.04 km/s) (Fig. 9A). Note that high-velocity metapelite can also be present. In Vp/Vs vs Vp space, the modelled eclogite and peridotite are also good fits to the measured Vp/Vs (1.72 ±0.04) (Fig. 9B). The average density (3.2 +/− 0.05 g/cm^3) fits well with the modelled peridotite (Fig. 9C). Modelled eclogite with between 15 to c. 55% garnet, 0% plagioclase, and between roughly 10 to 80% pyroxene fall within the range of uncertainty of the in situ Vp (7.9 ±0.17 km/s) (Fig. 7). The modelled peridotite can contain 0 to about 30% garnet, 0% plagioclase, and a range from 0 to nearly 100% pyroxene.

In the Central Range, at 50 km depth, the modelled velocities for the upper range of felsic and mafic granulite, biotite-poor metapelite, amphibolite, and the lower range of eclogite fit well with the in situ averages of Vp (7.1 +/− 0.19 km/s) and Vs (4.2 +/− 0.06 km/s) (Fig. 9A). In Vp/Vs versus Vp space, only one modelled metapelite velocity fits within the uncertainty range of the measured Vp/Vs (1.70 +/− 0.04) (Fig. 9B). With respect to density, only mafic granulite and mica-free metapelite fit fall within the range of uncertainty of the in situ average density (3.0 ±0.06 g/cm^3) (Fig. 9C). Modelled metapelite with up to 30% garnet, 30–45% garnet + sillimanite, and < 10% plagioclase falls within the range of uncertainty of the in situ Vp (7.1 +/− 0.19 km/s), whereas the felsic and mafic granulite can contain about 30 to 40% garnet, 20 to 45% plagioclase, and 20 to 30% pyroxene (Fig. 7). Amphibolite can contain 20 to 40% garnet, <10% plagioclase, and no pyroxene. The modelled eclogite can contain between 20 and 40% garnet, <20% plagioclase, and between roughly 10 to 40% pyroxene.

5.2. Chemical composition

For each modelled lithology, the major element composition was calculated and wt% SiO_2 plotted against Vp and Vp/Vs (Fig. 10A). Fig. 10A shows that at Vp <6.5 km/s there is a large range of possible SiO_2 compositions (40 to 79 wt%) that is associated with mica-bearing metapelite. Between roughly Vp 6.5–7.2 km/s, wt% SiO_2 ranges from 39 to 64 wt%. In this Vp range, amphibolite has overall lower wt% SiO_2 values, mafic and felsic granulite intermediate values, and metapelite higher values. At Vp 7.2–7.6 km/s, wt% SiO_2 ranges from approximately 41–55% (with one outlier of metapelite) and displays significant overlap between lithologies, although amphibolite, eclogite, and mafic granulite have lower values than felsic granulite and metapelite. At Vp > 7.6 km/s, wt% SiO_2 ranges from 39 to 56% with much overlap between the modelled mica-poor metapelite, eclogite, and peridotite. Fig. 10B shows that between Vp/Vs of 1.72–1.76 wt% SiO_2 can range from 39 to 79%, falling to <65% at Vp/Vs > 1.76. Within these ranges of Vp/Vs, there is a significant overlap of lithologies and consequently SiO_2 content.

To determine the average chemical composition of the Taiwan crust, all the modelled samples (minus marble) (see Supplementary data) whose Vp falls within the in situ Vp range of uncertainty (1σ) at 30, 40, and 50 km depth (Fig. 10A) are used to build a bulk rock composition (Table 2) from which the wt% oxides were calculated (Table 3). Beneath the Western Foothills, the calculated average wt% SiO_2 decreases with depth from 54.3 (±7.9) to 49.2 (+/− 4.8) to 46.1 (±3.6)%. Beneath the Central Range, it decreases from 61.0 (±7.9) to 54.6 (±7.7) to 49.2 (+/− 4.8)%. Note that, in the Central Range, the average Vp at 30 km depth (5.8 km/s) is much lower than that of the middle crust (6.3–6.9 km/s) so composition was not calculated for this depth. Calculated major element composition in wt% oxides and Mg# are given in Table 3.

6. Discussion

Modelled lithologies that match the in situ middle crust physical properties taken from the TAIGER regional data include felsic granulite, mica-bearing metapelite with <30% garnet + sillimanite, garnet-poor amphibolite, and mafic granulite. Marble, a common lithology at the surface in the Central Range (Stanley et al., 1981; Ernst, 1983; Ho, 1988; Lan et al., 2008) and intersected in borehole in Western Foothills (Jahn et al., 1992), does not fit with the in situ physical properties. There is a notable difference in the composition of the metapelite that fits the middle crustal Vp of the Western Foothills (<10% biotite +/−

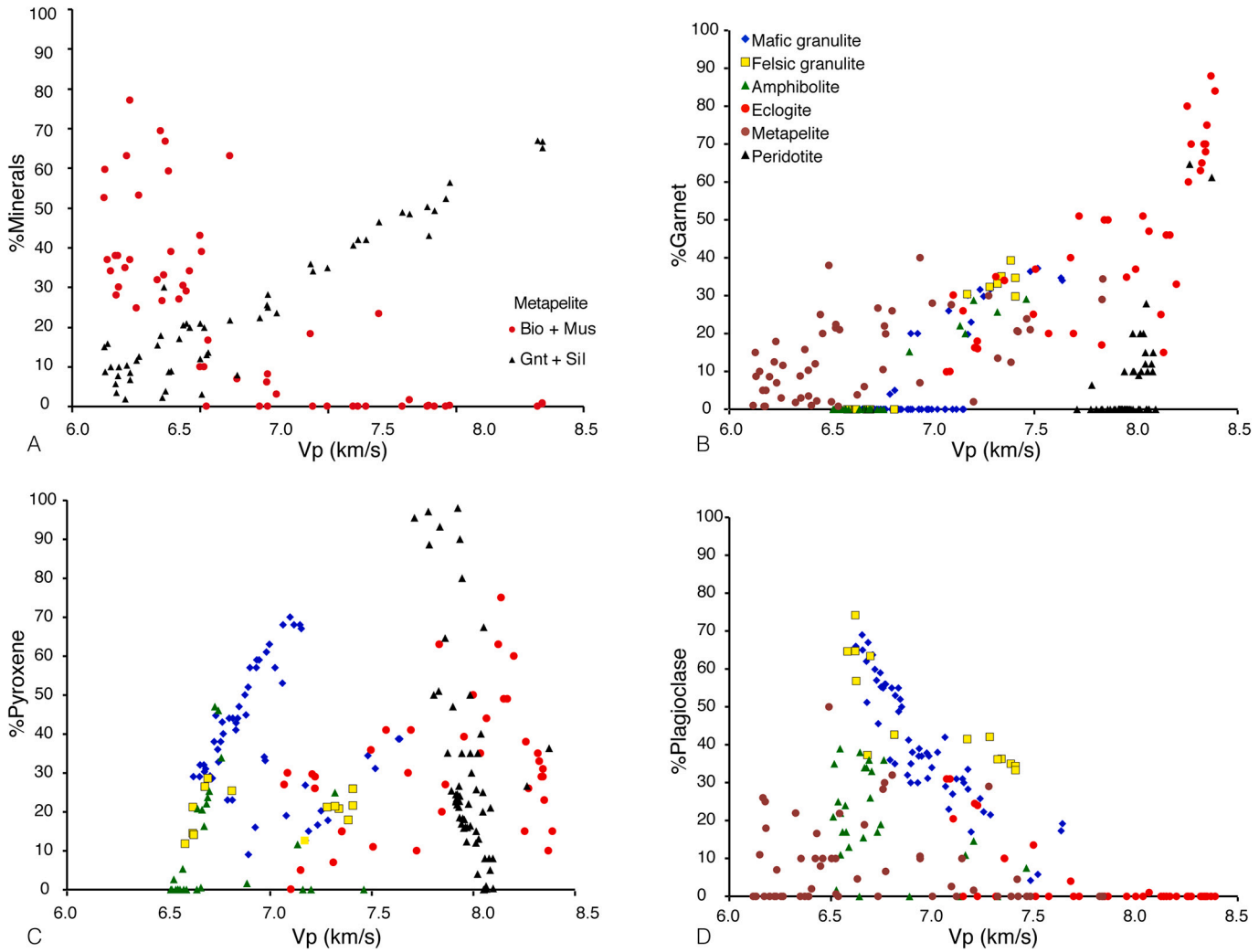

Fig. 7. A) Modal abundance (%) of biotite (Bio) + muscovite (Mus) and garnet (Gnt) + Sillimanite (Sil) in metapelite vs Vp. Vp is calculated with the AHM. B) Modal abundance (%) of garnet vs Vp for various lithologies modelled with AHM. C) Modal abundance (%) of pyroxene vs Vp for various lithologies modelled with AHM. D) Modal abundance (%) of plagioclase vs Vp for various lithologies modelled with AHM.

muscovite) compared to that in the Central Range (up to 80% biotite +/− muscovite). The lower crust may contain granulite facies felsic and mafic lithologies, and can be made up of a combination of garnet-bearing felsic and mafic granulite, mica-poor (<5%), garnet + sillimanite bearing metapelite, garnet amphibolite, and eclogite. Of the possible middle and lower crustal lithologies suggested by the modelling, xenoliths of amphibolite, metapelite, and marble have been reported from granitoids in the Central Range (Lo and Lee, 1981; Hung, 2010; Huang, 2013), further supporting the presence of our modelled lithologies in the middle and lower crust. To our knowledge, no crustal xenoliths have been reported from western Taiwan. The upper mantle below the Western Foothills can be made up of peridotite, eclogite, and possibly mica-free metapelite that contains 65–70% garnet + sillimanite. Mantle xenoliths have not been reported from western Taiwan, although spinel peridotite and minor spinel pyroxenite have been described from the Penghu Islands in the Taiwan Strait (Wang et al., 2003, 2010).

The physical properties of rocks are related to the aggregate sum of the volume percent of their mineral constituents, and so to their end-member composition (e.g., Rudnick and Jackson, 1995; Gao et al., 2000; Behn and Keleman, 2003). Individual minerals, even in small amounts, can have a significant effect on the physical properties of a rock (e.g., Kern, 1982; Holbrook et al., 1992; Kelemen and Holbrook, 1995; Kern et al., 1996; Behn and Keleman, 2003). For example, high-velocity minerals such as garnet and sillimanite can result in metapelite having a P-wave velocity and density that is typical of mantle values, whereas low-velocity minerals such as quartz, biotite, and plagioclase reduce the bulk rock physical properties (Figs. 7, and 9). Also, the models indicate that a modal abundance of biotite (+/−muscovite) in the range of c. 25–80% has a significant impact on low Vp (≤ 6.5 ±0.01 km/s) metapelite with <20% garnet + sillimanite (Fig. 7A). Higher Vp (>6.5 km/s), mica-bearing metapelite has >20% modal abundance of garnet + sillimanite. We interpret this relationship to indicate that the change from upper amphibolite facies (mica-bearing) to granulite facies (mica-free) can be interpreted from Vp in metapelite. The possible presence of both mica-rich and mica-free metapelite in Taiwan's middle crust (Figs. 6 and 8) is in keeping with our interpretation that this level of the crust is at upper amphibolite to granulite facies P and T conditions (Fig. 5).

Most lithologies show a significant increase in Vp with increased garnet content (Fig. 7B), although there are differences between lithologies that may reflect the garnet end-member composition (Table 1). For example, metapelite, whose garnet is richer in the lower velocity end-member almandine, shows only a weak increase in Vp with increased modal abundance of garnet (Fig. 7B), indicating that at Vp >6.5 +/− 0.1 km/s sillimanite has a more important effect on the wave-speed (Fig. 7A), and is therefore possibly a key contribution to the high Vp in Taiwan's middle and lower crust. Granulite, amphibolite, and

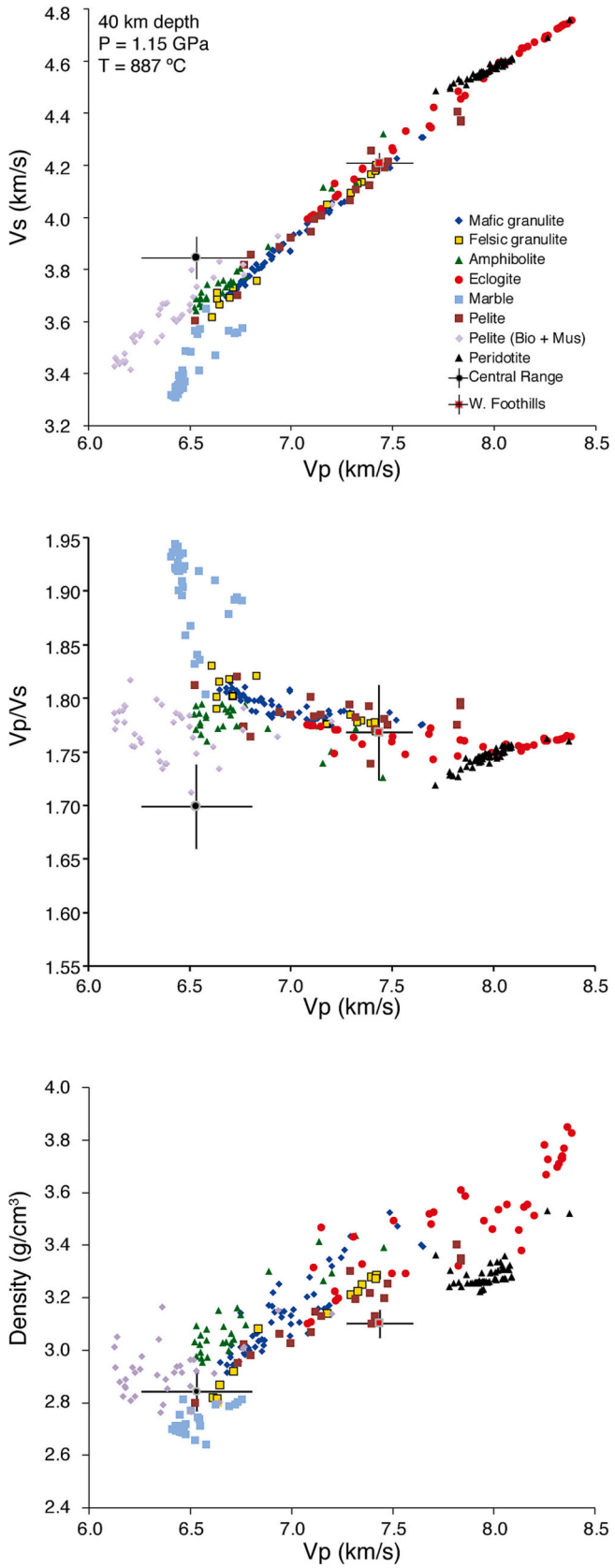

Fig. 8. Vs vs Vp, Vp/Vs vs Vp, and Density vs Vp plots for the model lithologies at 40 kn depth ($P = 1.15$ GPa) and $T = 887$ °C. The average in situ values for the Western Foothills and the Central Range are shown. Error bars are 1 σ.

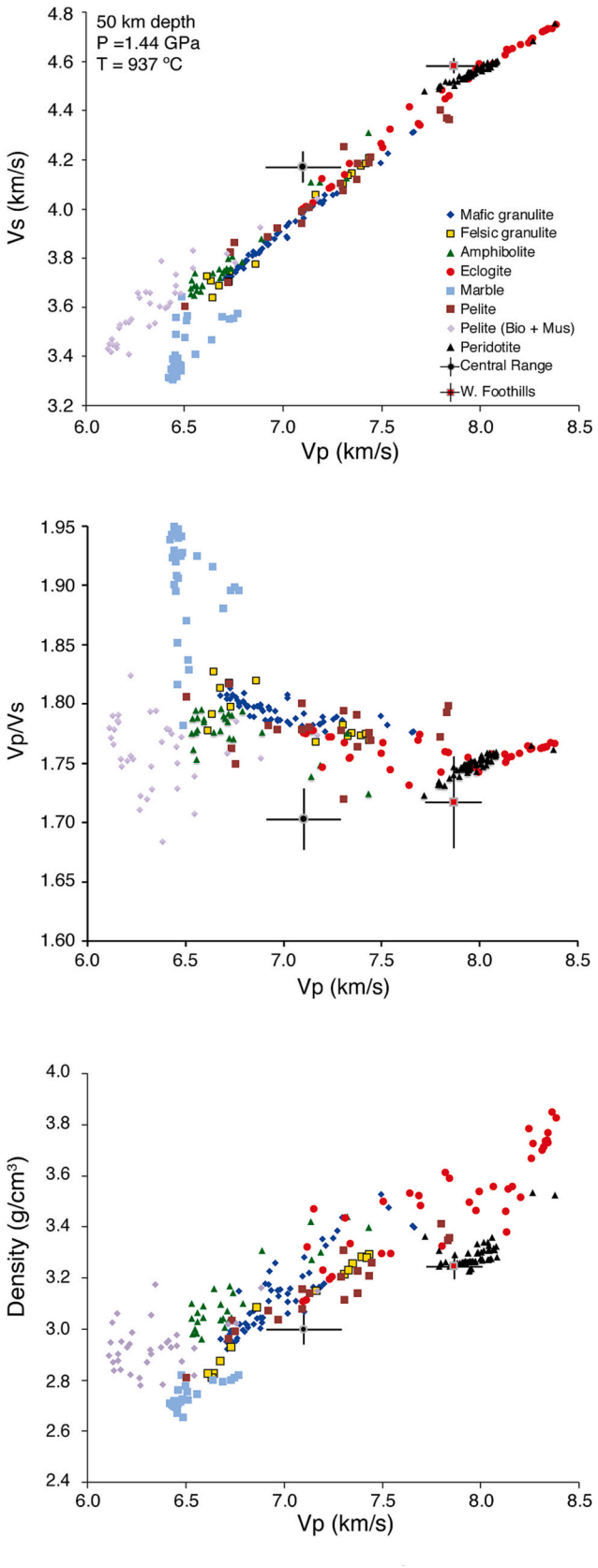

Fig. 9. Vs vs Vp, Vp/Vs vs Vp, and Density vs Vp plots for the model lithologies at 50 kn depth ($P = 1.44$ GPa) and $T = 937$ °C. The average in situ values for the Western Foothills and the Central Range are shown. Error bars are 1 σ.

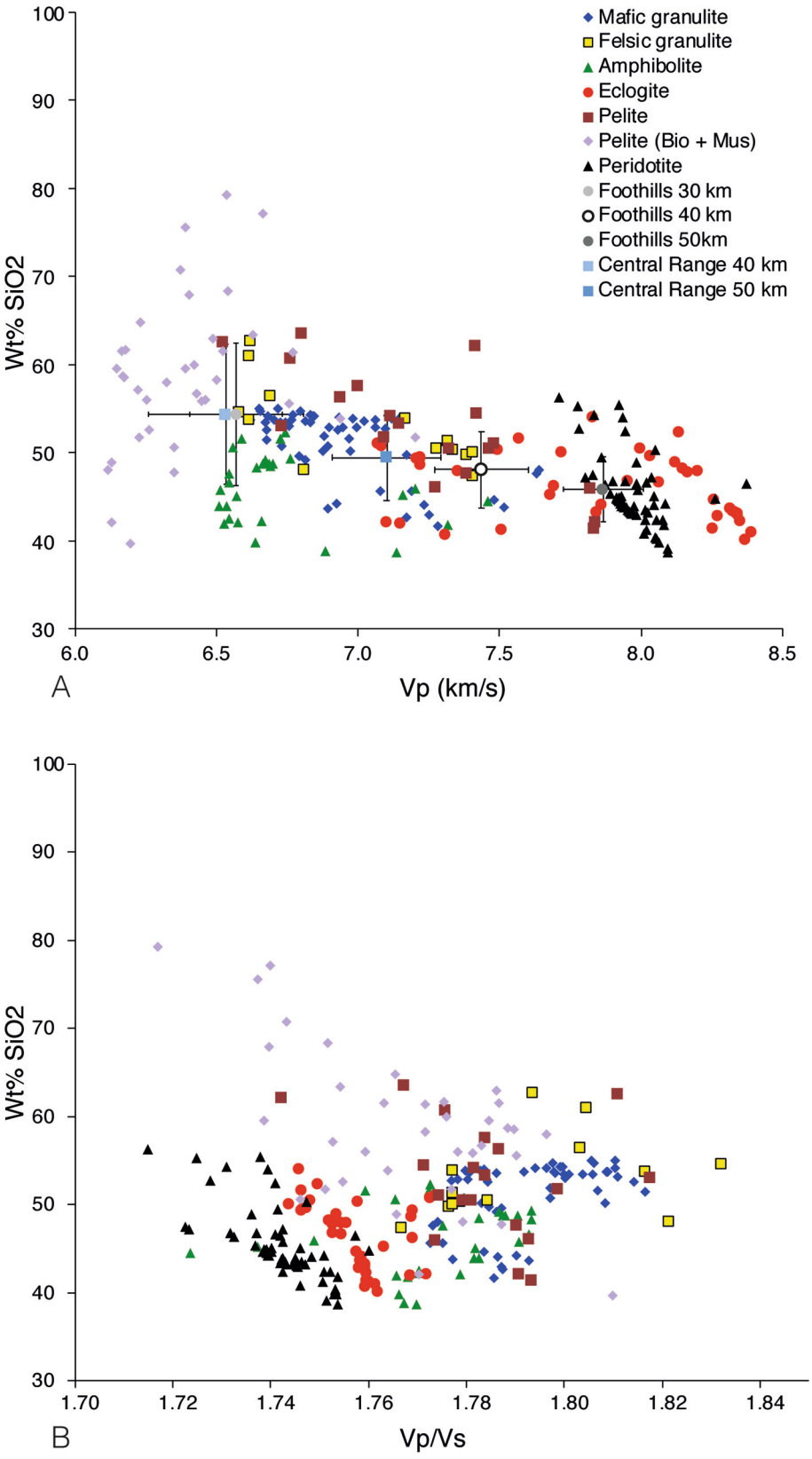

Fig. 10. A) Wt% SiO_2 vs Vp for the modelled samples. The average in situ Vp for the Western Foothills and the Central Range are shown. Error bars are 1 σ. The average Wt% SiO_2 is calculated from only those samples that fall within the error bars of the in situ Vp. B) Wt% SiO_2 vs Vp/Vs for the modelled samples. There is significant overlap between lithologies, with no clear correlation of SiO_2 content and Vp/Vs.

Table 2
Lithological composition for the calculation of wt% oxides.

	Western foothills			Central range		
	30 km	40 km	50 km	30 km[a]	40 km	50 km
Pelite	23	15	5	100	40	14
Mafic granulite	26	35	–	–	19	57
Felsic granulite	9	10	–	–	8	2
Amphibolite	42	10	–	–	33	7
Eclogite	–	30	15	–	–	20
Peridotite	–	–	80	–	–	–

[a] Determined for modelled P and T for 20 km depth.

eclogite, which are richer in the higher Vp end-members grossular and pyrope, show a marked increase in Vp with increased modal abundance of garnet. Therefore, we interpret Taiwan's lower crust (Vp 6.9–7.5) to have up to 40% garnet. Eclogite and metapelite of the crust/mantle transition zone (7.5 to 7.8 km/s) can contain between c. 17 and 50% garnet (Fig. 7B). Peridotite, which is rich in the medium-velocity pyrope end-member, shows almost no relationship between Vp and modal abundance of garnet (nor with pyroxene).

The AHM modelling further suggests that both the middle and lower crust of Taiwan have a mafic chemical composition, with an average wt % SiO_2 of 54 and 49%, and a Mg# of 51 and 41, respectively (Table 3). These values would change, becoming from mafic or felsic, with changes in the volume percent of each lithology used in the wt% oxide calculation (Table 2). For example, an amphibolite and a metapelite can have similar Vp, but their wt% SiO_2 can vary by >20%, and their Mg# 20 to 30 (e.g., Rudnick and Fountain, 1995; Christensen, 1996; Hacker et al., 2015). P- and S-wave anisotropy in Taiwan's middle and lower crust (Chen et al., 2003; Huang et al., 2015; Koulakov et al., 2015) can affect the calculated composition, since it is an important component in the overlap of wavespeeds between different rock types (e.g., Christensen and Mooney, 1995; Rudnick and Fountain, 1995; Hacker et al., 2015). Nevertheless, we feel that this calculation gives a reasonable estimate of the bulk rock chemical composition of Taiwan's middle and lower crust that matches it's in situ physical properties. Van Avendonk et al. (2014) also suggested that the composition of the lower crust (they define lower crust as having Vp 6.5–7.5 km/s) beneath Taiwan is mafic. The modelled SiO_2 values are similar to those of basalt (<54% SiO_2), but with lower Mg#'s than those of primitive basalt (Mg# >60) (terminology of Kelemen et al. (2003, 2014)). The modelled SiO_2 values for Taiwan are lower than those determined for the continental crust by Rudnick and Gao (2003, 2014) but are a close match to the mafic end-members of Hacker et al. (2015), and broadly similar to those modelled by Behn and Keleman (2003) for a warm geothermal gradient at similar values of Vp and depth. The Mg#'s are overall similar to those of Rudnick and Gao (2003, 2014) and Hacker et al. (2015), but are much less that those modelled by Behn and Keleman (2003) for 40 km and 50 km depth.

7. Conclusions

The AHM modelling carried out in this study indicates that Taiwan's middle crust is likely comprised of some combination of upper amphibolite to granulite facies felsic (biotite-poor metapelite, garnet-poor felsic granulite) and mafic lithologies (mafic granulite, amphibolite), and possibly marble. The lower crust is likely comprised of mafic granulite, garnet-rich felsic granulite, biotite-free metapelite, and eclogite. The modelled wt% major oxide composition suggests that both the middle and lower crust have an overall mafic chemical composition. Much more so than those calculated globally for the middle and lower crust. It should be noted that there is uncertainty in the values that we calculate that is due to the P- and S-wave anisotropy in Taiwan's middle

Table 3
Average in situ Vp, Vs, Vp/Vs, and density (ρ) from TAIGER data. Modelled[a] composition compared to global middle and lower crust compositon.

	Western Foothills						Central range						Hacker et al[b]		Rudnick & Gao		Behn and Kelemen[c]	
	30 km		40 km		50 km		30 km		40 km		50 km		Middle	Lower	Middle	Lower	40 km	
	avg	SD	avg	SD	avg	SD	avg	SD	avg	SD	avg	SD	avg	avg	avg	avg	avg	avg
Vp (km/s)	6.6	0.17	7.4	0.18	7.9	0.17	5.8	0.28	6.5	0.27	7.1	0.19	6.73	7.18			7.2/6.5	7.6/7.1
Vs (km/s)	3.8	0.05	4.2	0.04	4.6	0.04	3.6	0.12	3.9	0.08	4.2	0.06	3.83	4.07				
Vp/Vs	1.74	0.04	1.77	0.04	1.72	0.04	1.62	0.04	1.70	0.04	1.70	0.03	1.76	1.76				
ρ (g/cm^3)	2.9	0.05	3.1	0.06	3.2	0.05	2.7	0.06	2.8	0.08	3.0	0.06	2.99	3.19				
SiO_2 (wt%)	54.3	7.9	49.2	4.8	46.1	3.6	–	–	54.6	7.7	49.2	4.8	53.1	48.6	63.5	53.4	49.0/59.7	41.4/50.1
Al_2O_3 (wt%)	16.1	3.1	17.1	5.4	5.4	8.3	–	–	16.9	3.5	15.9	5.3	16.7	18.1	15.0	16.9	18.9/16.8	21.8/18.3
TiO_2 (wt%)	0.6	0.7	1.0	1.1	0.5	0.9	–	–	0.6	0.6	1.1	1.0	1.26	1.40	0.69	0.82		
$FeO_{(T)}$ (wt%)	10.3	3.2	13.5	3.5	9.1	4.1	–	–	10.0	2.9	13.9	3.5	10.32	10.44	6.02	8.57	6.5/8.2	5.5/7.0
MgO (wt%)	6.0	2.3	6.0	3.2	33.3	16.4	–	–	5.9	2.3	6.9	3.4	5.98	6.87	3.59	7.24	12.3/5.2	15.7/12.6
CaO (wt%)	7.4	4.0	9.7	3.8	5.0	6.3	–	–	6.6	4.3	9.6	3.4	7.48	10.11	5.25	9.59	9.3/4.0	11.1/7.8
Na_2O (wt%)	2.8	1.3	2.2	1.1	0.5	0.9	–	–	2.5	1.5	2.3	1.0	3.38	2.85	3.39	2.65	3.2/4.0	3.7/3.3
K_2O (wt%)	1.5	1.8	0.9	1.5	0.6	1.1	–	–	2.2	2.4	0.8	1.5	1.29	1.22	2.30	0.61	0.9/2.1	0.8/1.0
Mg#	49.9	9.9	41.2	16.2	79.7	23.0	–	–	50.0	10.5	44.2	15.9	51.0	54.0	51.5	60.0	77.1/53.1	83.6/76.2

[a] Calculated from all lithologies that fall within the 1σ uncertainty range of the average in situ Vp at each depth interval.
[b] Lowest wt% SiO_2 lower and middle crust from table 4 of Hacker et al. (2015).
[c] For a warm continental geotherm compared to WF/CR with the same average Vp. Behn and Keleman temperatures are lower than in Taiwan.

and lower crust. Furthermore, the modelling reinforces the evaluation of Hacker et al. (2015) that describing the crust as mafic or felsic on the basis of seismic wavespeeds should be done with caution, since a high modal abundance of minerals such as garnet and sillimanite can elevate the wavespeeds of a metapelite (a felsic rock) to those of mafic rocks such as eclogite or peridotite. To better asses this concern, the AHM models provide possible constraints on the major phase mineralogy of each lithology, and how these minerals affect the physical properties of the rocks that are being interpreted to occur in situ in Taiwan.

CRediT authorship contribution statement

D. Brown: Writing – review & editing, Writing – original draft, Visualization, Validation, Supervision, Resources, Project administration, Methodology, Investigation, Funding acquisition, Formal analysis, Data curation, Conceptualization. **G. Camanni:** Writing – review & editing, Writing – original draft, Visualization, Methodology, Investigation, Formal analysis. **H. Kuo-Chen:** Writing – review & editing, Writing – original draft, Validation, Resources, Methodology, Investigation, Formal analysis, Data curation. **J. Alvarez-Marron:** Writing – review & editing, Writing – original draft, Project administration, Funding acquisition, Formal analysis.

Declaration of Competing Interest

The authors declare that they have no known competing financial interests or personal relationships that could have appeared to influence the work reported in this paper.

Data availability

Data will be made available on request.

Acknowledgements

This publication if part of the I + D + i project PID2022-139422NB-I00 financed by MCIN/AEI/ 10.13039/501100011033 and by FEDER Una manera de hacer Europa. Kuo-Chen and Brown wish to acknowledge visiting researcher grant NSTC 112-2811-M-002-006. Comments on an earlier version of the manuscript by Dr. C—H. Tsai helped clarify aspects of the text. The comments of two anonymous reviewers helped to improve the paper.

Appendix A. Supplementary data

Supplementary data to this article can be found online at https://doi.org/10.1016/j.tecto.2023.230160.

References

Abers, G.A., Hacker, B.R., 2016. A MATHLAB toolbox and Excel workbook for calculating the densities, seismic wave speeds, and major element composition of minerals and rocks at pressure and temperature. Geochem. Geophys. Geosyst. 17, 616–624.

Behn, M.D., Keleman, P.B., 2003. Relationship between seismic P-wave velocity and the composition of anhydrous igneous and meta-igneous rocks. Geochem. Geophys. Geosyst. 4, 1041.

Bertrand, E.A., Unsworth, M.J., Chiang, C.-W., Chen, C.-S., Chen, C.-C., Wu, F.T., Turkoglu, E., Hsu, H.-L., Hill, G.J., 2009. Magnetotelluric evidence for thick-skinned tectonics in central Taiwan. Geology. 37, 711–714.

Bertrand, E.A., Unsworth, M.J., Chiang, C.-W., Chen, C.-S., Chen, C.-C., Wu, F.T., Turkoglu, E., Hsu, H.-L., Hill, G.J., 2012. Magnetotelluric imaging beneath the Taiwan orogen: an arc-continent collision. J. Geophys. Res. 117, B01402.

Boyd, O.S., 2020. Temperature model in support of the U.S. Geological Survey National Crustal Model for seismic hazard and studies. In: U.S.G.S. Open-file Report 2019-1121, 15 p.

Brocher, T.M., 2005. Empirical relations between elastic wavespeeds and density in the Earth's crust. Bull. Seismol. Soc. Am. 95, 2081–2092.

Brown, D., Carbonell, R., Kukkonen, I., Ayala, C., Golovonova, I., 2003. Composition of the Uralide crust from seismic velocity (Vp, Vs), heat flow, gravity, and magnetic data. Earth Planet. Sci. Lett. 210, 333–349.

Brown, D., Alvarez-Marron, J., Schimmel, M., Wu, Y.-M., Camanni, G., 2012. The structure and kinematics of the Central Taiwan mountain belt derived from geological and seismicity data. Tectonics 31. https://doi.org/10.1029/2012TC003156.

Brown, D., Wu, Y.-M., Feng, K.-F., Chao, W.-A., Huang, H.-H., 2015. Imaging high-pressure rock exhumation in eastern Taiwan. Geology 43, 651–654.

Brown, D., Alvarez-Marron, J., Camanni, G., Biete, C., Kuo-Chen, H., Wu, Y.-M., 2022. Structure of the south-central Taiwan fold-and-thrust belt: texting the viability of the model. Earth Sci. Rev. 231, 104094.

Brownlee, S.J., Hacker, B.R., Salisbury, M., Seward, G., Little, T.A., Baldwin, S.L., Abers, G.A., 2011. Predicted velocity and density structure of the exhuming Papua New Guinea ultrahigh-pressure terrane. J. Geophys. Res. 116, B08206.

Carbonell, R., Levander, A., Kind, R., 2013. The Mohorovicic discontinuity beneath the continental crust: an overview of seismic constraints. Tectonophysics. 609, 353–376.

Chen, C.-H., Ho, H.-C., Shea, K.-S., Lo, W., Lin, W.-H., Chang, H.-C., Huang, C.-S., Lin, C.-W., Chen, G.-H., Yang, C.-N., Lee, Y.-H., 2000. Geological Map of Taiwan. 1:500,000 scale. Central Geol. Sur, Taiwan.

Chen, C.-H., Chen, Y.-H., Yen, H.-Y., Yu, G.-K., 2003. Lateral variations of Pn velocity and anisotropy in Taiwan from travel-time tomography. Earth Planets Space 55, 223–230.

Chen, K.-X., Kuo-Chen, H., Brown, D., Li, Q., Ye, Z., Liang, W.-T., Wang, C.-Y., Yao, H., 2016. Three-dimensional ambient noise tomography across the Taiwan Strait: the structure of a magma-poor rifted margin. Tectonics 35, 1782–1792.

Chiu, H.-T., 1975. Miocene stratigraphy and its relation to the Palaeogene rocks in west-central Taiwan. Petrol. Geol. Taiwan 12, 51–80.

Christensen, N.I., 1996. Poisson's ratio and crustal seismology. J. Geophys. Res. 101, 3139–3156.

Christensen, N.I., Mooney, W.D., 1995. Seismic velocity structure and composition of the continental crust: a global view. J. Geophys. Res. 100, 9761–9788.

Ernst, W.G., 1983. Mineral parageneses in metamorphic rocks exposed along the Tailuko Gorge, Central Mountain Range, Taiwan. J. Met. Geol. 1, 305–329.

Ernst, W.G., Jahn, B.-M., 1987. Crustal accretion and metamorphism in Taiwan, a port-Paleozoic mobile belt. Phil. Trans. R. Soc. Lond. Ser. A. Math. Phys. Sci. 321, 129–161.

Gao, S., Kern, H., Liu, Y.-S., Jin, S.-Y., Popp, T., Jin, Z.-M., Feng, J.-L., Sun, M., Zhao, Z.-B., 2000. Measured and calculated seismic velocities and densities for granulites from xenolith occurrences and adjacent exposed lower crustal sections: a comparative study from the North China craton. J. Geophys. Res. 105, 18965–18976.

Giese, P., 2005. Moho discontinuity. In: Selly, R.C., Cocks, L.R.M., Plimer, I.R. (Eds.), Encyclopedia of Geology, vol. 3. Elsevier Academic Press, Oxford, pp. 645–659.

Hacker, B.R., Abers, G.A., 2003. Subduction Factory 3: an Excel worksheet and macro for calculating the densities, seismic wave speeds, and H_2O contents of minerals and rocks at pressure and temperature. Geochem. Geophys. Geosyst. https://doi.org/10.1029/2003GC0000614, 5.

Hacker, B.R., Keleman, P.B., Behn, M.D., 2015. Continental Lower Crust. Ann. Rev. Earth Plant. Sci. 43, 167–205.

Ho, C.-S., 1988. An Introduction to the Geology of Taiwan: Explanatory Text of the Geological Map of Taiwan. Central Geol. Sur, Taipei, Taiwan.

Ho, G.-R., Byrne, T.B., Lee, J.-C., Mesalles, L., Lin, C.-W., Lo, W., Chang, C.-P., 2022. A new interpretation of the metamorphic core in the Taiwan orogen: a regional-scale, left lateral shear zone that accommodated highly oblique plate convergence in the Plio-Pleistocene. Tectonophysics. 833, 229332.

Holbrook, W.S., Mooney, W.D., Christensen, N.I., 1992. The seismic velocity structure of the deep continental crust. In: Fountain, D.M., Arculus, R., Kay, R. (Eds.), Continental Lower Crust. Elsevier, Amsterdam, pp. 1–43.

Hsieh, H.-H., Chen, C.-H., Lin, P.-Y., Yen, H.-Y., 2014. Curie point depth from spectral analysis of magnetic data in Taiwan. J. Asian Earth Sci. 90, 26–33.

Huang, J.W., 2013. Petrologic Characterization of Amphibolites and Mafic Enclaves in Metagranitoids in the Nanao Area, NE Taiwan. National Dong Hwa University. MS thesis, 172 p (in Chinese with English abstract).

Huang, C.-Y., Yen, Y., Zhao, Q.H., Lin, C.-T., 2012. Cenozoic stratigraphy of Taiwan: window into rifting, stratigraphy and paleoceanography of South China Sea. Chinese Sci. Bull. 57, 3130–3149.

Huang, H.-H., Wu, Y.-M., Song, X., Chang, C.-H., Kuo-Chen, H., Lee, S.-J., 2014a. Investigating the lithospheric structures beneath Taiwan region by nonlinear joint inversion of local and teleseismic P-wave data: slab continuity and deflection. Geophys. Res. Lett. 41 https://doi.org/10.1002/2014GL061115.

Huang, H.-H., Wu, Y.-M., Song, X., Chang, C.-H., Lee, S.-J., Chang, T.-M., Hsieh, H.-H., 2014b. Joint Vp and Vs tomography of Taiwan: implications for subduction-collision orogeny. Earth Planet. Sci. Lett. 392, 177–191.

Huang, T.-Y., Gung, Y., Kuo, B.-Y., Chaio, L.-Y., Chen, Y.-N., 2015. Layered deformation in the Taiwan orogen. Science. 349, 720–723.

Hung, C.F., 2010. Metamorphism and Geological Implications of Garnet-Bearing Rocks in the Hoping Area, Eastern Taiwan, National Dong Hwa University. M.S. Thesis, 127 p (in Chinese with English abstract).

Hung, J.-H., Ma, K.-F., Wang, C.-Y., Ito, H., Lin, W., Yeh, E.-C., 2009. Subsurface structure, physical properties, fault-zone characteristics and stress state in scientific drill holes of Taiwan Chelungpu fault dripping project. Tectonophysics. 466, 307–321.

Hyndman, R.D., Peacock, S.M., 2003. Serpentinization of the forearc mantle. Earth Planet. Sci. Lett. 212, 417–432.

Jahn, B.-M., Chi, W.-R., Yui, T.-F., 1992. A Late Permian formation of Taiwan marbles from Chia-Li well No.1: Pb-Pb isochron and Sr isotopic evidence, and its regional geological significance. J. Geol. Soc. China 35, 193–218.

Jarchow, C.M., Thompson, G.A., 1989. The nature of the Mohorovicic discontinuity. Annu. Rev. Earth Planet. Sci. 17, 475–506.
Kelemen, P.B., Holbrook, W.S., 1995. Origin of thick, high-velocity igneous crust along the U.S. east coast margin. J. Geophys. Res. 100, 10077–10094.
Kelemen, P.B., Hanghoj, K., Greene, A.R., 2003. One view of the geochemistry of subduction-related magmatic arcs, with an emphasis on primitive andesite and lower crust. In: Holland, H.D., Turekian, K.K. (Eds.), Treatise on Geochemistry, The Crust, Vol. 3. Elsevier-Pergammon, Oxford, U.K., pp. 593–659
Kelemen, P.B., Hanghoj, K., Greene, A.R., 2014. One view of the geochemistry of subduction-related magmatic arcs, with an emphasis on primitive andesite and lower crust. In: Holland, H.D., Turekian, K.K. (Eds.), Treatise on Geochemistry, The Crust, Vol. 4. Elsevier-Pergammon, Oxford, U.K., pp. 749–806
Kern, H., 1982. Elastic-wave velocity in crustal and mantle rocks at high pressure and temperature: the role of the high-low quartz transition and of dehydration reactions. Phys. Earth Planet. Int. 29, 12–23.
Kern, H., Gao, S., Liu, Q.-S., 1996. Seismic properties and densities of the middle and lower crustal rocks exposed along the North China Geoscience Transect. Earth Planet. Sci. Lett. 139, 439–455.
Kim, K.-H., Chiu, J.-M., Pujol, J., Chen, K.-C., Huang, B.-S., Yeh, Y.-H., Shen, P., 2005. Three-dimensional Vp and Vs structural models associated with the active subduction and collision tectonics in the Taiwan region. Geophys. J. Int. 162, 204–220.
Koulakov, I., Jakovlev, A., Wu, Y.-M., Dobretsov, N.L., El Khrepy, S., Al-Arifi, N., 2015. Three-dimensional seismic anisotropy in the crust and uppermost mantle beneath the Taiwan area revealed by passive source tomography. J. Geophys. Res. 120 https://doi.org/10.1002/2015JB012408.
Kuan, M.Y., 1971. Advanced study on the subsurface geology of the Chinshui gas field, Miaoli, Taiwan. Petrol. Geol. Taiwan. 8, 47–64.
Kuo, Y.-W., Wang, C.-Y., Kuo-Chen, H., Jim, X., Cai, H.-T., Lin, J.-Y., Wu, F.T., Yen, H.-Y., Huang, B.-S., Liang, W.-T., Okaya, D., Brown, L., 2016. Crustal structures from the Wuyi-Yunkai orogen to the Taiwan orogen: the onshore-offshore wide-angle seismic experiments of the TAIGER and ATSEE projects. Tectonophysics. 692, 164–180.
Kuo-Chen, H., Wu, F.T., Roecker, S.W., 2012a. Three-dimensional P velocity structures of the lithosphere beneath Taiwan from the analysis of TAIGER and related seismic data sets. J. Geophys. Res. 117 https://doi.org/10.1029/2011JB009108.
Kuo-Chen, H., Wu, F.T., Jenkins, D.M., Mechie, J., Roecker, S.W., Wang, C.-Y., Huang, B.-S., 2012b. Seismic evidence for the α-β quartz transition beneath Taiwan from Vp/Vs tomography. Geophys. Res. Lett. 39, L22302.
Lan, C.-Y., Lee, C.-S., Yui, T.-F., Chu, H.-T., Jahn, B.-M., 2008. The tectono-thermal events of Taiwan and their relationship with SE China. Terr. Atmos. Ocean. Sci. 19, 257–278.
Lee, C.R., Cheng, W.-T., 1986. Preliminary heat flow measurements in Taiwan. In: Fourth Circum-Pacific Energy and Minerals Conference: August 17–22, Singapore.
Li, C.-F., Zhou, Z., Li, J., Hao, H., Geng, J., 2007. Structures of the northeasternmost South China Sea continental margin and ocean basin: geophysical constraints and tectonic implications. Mar. Geophys. Res. 28, 59–79.
Lin, A., Watts, A., Hesselbo, P., 2003. Cenozoic stratigraphy and subsidence history of the South China Sea margin in the Taiwan region. Basin Res. 15, 453–478.
Liu, Y., Li, C.-F., Qiu, X., Zhang, J., 2023. Vp/Vs ratios beneath a hyper-extended failed rift support a magma-poor continental margin in the northeastern South China Sea. Tectonophysics 846. https://doi.org/10.1016/j.tecto.2022.229652.
Llana-Funez, S., Brown, D., 2012. Contribution of crustallographic preferred orientation to seismic anisotropy across a surface analog of the continental Moho at Cabo Ortegal, Spain. GSA Bull. 124, 1495–1513.
Lo, C.-H., Lee, C.-W., 1981. Marble enclave in the Chipan granitic gneiss, Hualien, eastern Taiwan. Proc. Geol. Soc. China. 24, 137–140.
Lo, Y.-T., Huang, H.-H., Yen, H.-Y., 2021. Probing depth origin of gravity anomalies in Taiwan through 3-D coherent velocity model, Terre. Atmos. Oceanic Sci. https://doi.org/10.3319/TAO.2021.04.30.01.
Marini, L., Manzella, A., 2005. Possible seismic signature of the α-β quartz transition in the lithosphere of Southern Tuscany (Italy). J. Vol. Geothermal Res. 148, 81–97.
Miller, D.J., Christensen, N.I., 1994. Seismic signature and geochemistry of an island arc: a multidisciplinary study of the Kohistan accreted terrane, northern Pakistan. J. Geophys. Res. 99, 11623–11642.
Morozov, I.B., Christensen, N.I., Smithson, S.B., Hollister, L.S., 2003. Seismic and laboratory constraints on crustal formation in a former continental arc (ACCRETE, southeastern Alaska and western British Columbia). J. Geophys. Res. 108, 16-1–16-9.
Peng, Z., Redfern, A.T., 2013. Mechanical properties of the quartz at the a-b phase transition: Implications for tectonic and seismic anomalies. G-Cubed 14, 18–28.
Rudnick, R.L., Fountain, D.M., 1995. Nature and composition of the continental crust: a lower crustal perspective. Rev. Geophys. 33, 267–309.
Rudnick, R.L., Gao, S., 2003. Composition of the Continental Crust. In: Holland, H.D., Turekin, K.K. (Eds.), Treatise on Geochemistry, vol. 3. Elsevier-Pergammon, Oxford, pp. 1–64.
Rudnick, R., Gao, S., 2014. In: Holland, H.D., Turekian, K.K. (Eds.), Treatise on Geochemistry, , 2nd ed.4. The Crust, Oxford, UK.
Rudnick, R.L., Jackson, I., 1995. Measured and calculated elastic wave speeds in partially equilibrated mafic granulite xenoliths: implications for the properties of an underplated lower continental crust. J. Geophys. Res. 100, 10211–10218.
Schutt, D.L., Lowry, A.R., Buehler, J.S., 2018. Moho temperature and mobility of the lower crust in the western United States. Geology. 46, 219–222.
Shaw, C.-L., 1996. Stratigraphic correlation and isopach maps of the Western Taiwan Basin. Terr. Atmos. Ocean. Sci. 7, 333–360.
Sibuet, J.C., Hsu, S.-K., 1997. Geodynamic of the Taiwan arc-continent collision. Tectonophysics 274, 221–252.
Sibuet, J.C., Hsu, S.-K., 2004. How was Taiwan created? Tectonophysics 379, 159–181.
Stanley, R.S., Hill, L.B., Chang, H.-C., Hu, H.-N., 1981. A transect through the metamorphic core of the Central Mountains, southern Taiwan. Mem. Geol. Soc. China 4, 443–473.
Tanaka, H., Chen, W.M., Kawabata, K., Urata, N., 2007. Thermal properties across the Chelungpu fault zone and evaluations of positive thermal anomaly on the slip zones: are these resuduals of heat from faulting? Geophys. Res. Lett. 34, L01309.
Taylor, R.L., Rutter, E.H., Nippress, S.E.J., Brodie, K.H., 2015. Seismic velocity modelling of the Carboneras Fault Zone, SE Spain. Tectonophysics 646, 20–35.
Teng, L.-S., 1992. Geotectonic evolution of Tertiary continental margin basins of Taiwan. Petrol. Geol. Taiwan 27, 1–19.
Teng, L.-S., Lin, A.-T., 2004. Cenozoic tectonics of the China continental margin; Insights from Taiwan. In: Malpas, J., Fletcher, C.J.N., Ali, J.R., Aitchison, J.C. (Eds.), Aspects of the Tectonic Evolution of China, Geol. Soc. London, Spec. Pub, 226, pp. 313–332.
Tsai, C.-H., Iizuka, Y., Ernst, W.G., 2013. Diverse mineral compositions, textures, and metamorphic P-T conditions of the glaucophane-bearing rocks in the Tamayen mélange, Yuli belt, eastern Taiwan. J. Asian Earth Sci. 63, 218–233.
Van Avendonk, H.J.A., Kuo-Chen, H., McIntosh, K.D., Lavier, L.L., Okaya, D.A., Wu, F.T., Wang, C.-Y., Lee, C.-S., Liu, C.-S., 2014. Deep crustal structure of an arc-continent collision: constraints from seismic traveltimes in Central Taiwan and the Philippine Sea. J. Geophys. Res. 119, 8397–8416.
Wang, K.-L., O'Reilly, S.Y., Griffin, W.L., Chung, S.-L., Pearson, N.J., 2003. Proterozoic mantle lithosphere =beneath the extended margin of the South China block: in situ Re-Os evidence. Geology. 31, 709–712.
Wang, K.-L., O'Reilly, S.Y., Honda, M., Matsumoto, T., Griffin, W.L., Pearson, N.J., Zhang, M., 2010. Co-rich sulfides in mantle peridotites from Penghu Islands, Taiwan: footprints of Proterozoic mantle plumes under the Cathaysia Block. J. Asian Earth Sci. 37, 229–245.
Wu, Y.-M., Chang, C.-H., Zhao, L., Shyu, J.B.H., Chen, Y.-G., Sieh, K., Avouac, J.P., 2007. Seismic tomography of Taiwan: improved constraints from a dense network of strong motion stations. J. Geophys. Res. 112 https://doi.org/10.1029/2007JB004983.
Wu, S.-K., Chi, W.-C., Hsu, S.-M., Ke, C.-C., Wang, Y., 2013. Shallow crustal thermal structures of central Taiwan foothills region. Terr. Atmos. Ocean. Sci. 24, 695–707.
Zappone, A.S., Benson, P.M., 2013. Effect of phase transitions on seismic properties of metapelites: a new high-termperture laboratory calibration. Geology 41, 463–466.